Relating the electrochemical behavior of Birnessite to the morphology and specific surface: interest of studying the surface reactivity

Alexia Lemoine, Ronan Invernizzi, Germain Salvato Vallverdu, Jacob Olchowka, Liliane Guerlou-Demourgues, Isabelle Baraille, Delphine Flahaut

Relying the electrochemical behavior of birnessite to the morphology and specific surface: interest of studying the surface reactivity.

Alexia Lemoine[1], Ronan Invernizzi[2,3], Germain Salvato Vallverdu[1,3], Jacob Olchowka[2,3,4], Liliane Guerlou-Demourgues[2,3,4], Isabelle Baraille[1,3], Delphine Flahaut[1,3]**

1. Université de Pau et des Pays de l'Adour, E2S UPPA, CNRS, IPREM, UMR 5254, 64000 Pau, France
2. Univ. Bordeaux, CNRS, Bordeaux INP, ICMCB, UMR 5026, F-33600 Pessac, France
3. RS2E, Réseau Français sur le Stockage Electrochimique de l'Energie, FR CNRS 3459, F-80039 Amiens Cedex 1, France
4. ALISTORE-ERI European Research Institute, FR CNRS 3104, F-80039 Amiens Cedex 1, France

KEYWORDS: supercapacitors, energy storage, MnO_2, surface reactivity, morphology

ABSTRACT.

This article focuses on the understanding of the link between morphologies, specific surface of well-known birnessites with electrochemical performances by studying the surface reactivity of each material. Our study is especially dedicated to point out the impact of the materials surface on the faradaic and pseudocapacitive mechanisms involved in the energy storage of the supercapacitors. For this purpose, a multiscale study was carried out on three birnessites, non-protonated (Na-MnO_2, K-MnO_2 and HT-MnO_2) and protonated (H_{Na}-MnO_2, H_K-MnO_2 and H_{HT}-MnO_2), to ensure the investigation of the surface reactivity on birnessites for each step of the nanocomposite conception based on birnessite. Scanning electron microscopy (SEM) was used to characterize the morphology of the materials. Coupling X-ray photoemission spectroscopy (XPS) and SO_2 gas probe adsorption are especially devoted to determine the nature of active sites and the electronic structure of the materials surface. Thus, we put in evidence that the surface properties, as specific surface area and surface active sites, are linked to the electrochemical mechanism (faradaic or pseudocapacitive) of storage depending of the scan rate. We show that the sites concentration determined by XPS can be directly linked to the contribution of the pseudocapacitive mechanism observed at low and moderate scan rates. As for the capacitive mechanism is discriminated at high scan rate, its contribution is related to the BET surface. The largest specific surface is obtained for the H_K-MnO_2 with its eroded veails (85 m^2/g). Redox reactivity have been evaluated from XPS quantification comparing the S/M values, i.e. at. % of S / at% of Mn. HT-MnO_2, its protonated derivative H_{HT}-MnO_2 and Na-MnO_2 exhibit the largest redox reactivity, with respectively, S/M values of 0.49, 0.46 and 0.31, according to their smooth platelets morphology. Except for the high temperature birnessite, the change of morphology after the protonation makes decrease the concentration of redox active sites while BET surface is increasing. This work point

out that the H_K-MnO_2 presents the best performances, 46.6 F/g at 100 mV/s, to be used as an electrode material in supercapacitor storage systems.

INTRODUCTION

With the increasing demand for energy storage devices, especially in applications that require high power density, supercapacitors appear as perfectly adapted storage systems [1,2]. The most widespread systems currently used are electric double layer capacitors (EDLCs), however they have limits in terms of energy density delivered (3-10 W h/kg), which is a brake for a wider application [3,4]. This limitation is mainly caused by the charge storage mode, which only consists in adsorbing and desorbing ions from the electrolyte on the surface of carbon electrodes, so that the capacity is dependent on the accessible specific surface area (SSA). One of the solutions to increase the energy density is to involve another storage mechanism in addition to the electrostatic one by replacing one of the carbon electrodes by a faradaic or pseudo-capacitive electrode material, which leads to hybrid or asymmetric supercapacitors. [5–7]

A pseudo-capacitive material involves charge storage through rapid and reversible redox reactions at the surface of the material. This process allows to increase the energy density while keeping a high power density. In the literature, several metal oxides are known for their pseudo-capacitive property such as RuO_2, $FeWO_4$ or MnO_2 [8–11]. The nanostructuration of the material is an essential criterion to increase the electrolyte/electrode interface and facilitate the access of the surface active sites. Since the oxidation-reduction reactions are essentially performed on the surface, this is a way to optimize the electrochemical performances. In the goal to elaborate a material with optimized performance, we need to understand the parameters that influence the surface reactions types that directly affect the electrochemical performance. Several investigations[12] are performed in this study such as surface and morphology characterization, as well as surface reactivity.

Birnessite δ-MnO_2 is well known for its interesting properties as positive electrode material in supercapacitors due to its promising pseudo-capacitive behaviour [13]. Its lamellar structure, based on a stacking of MnO_2 slabs, is very versatile and can lead to a large panel of composition for the interlamellar space as well as for the metallic slab (possibility of vacancies and various Mn oxidation states). In this work, a complete study is carried out on three birnessites with various compositions and morphologies designated as Na-MnO_2, K-MnO_2 and HT-MnO_2, as well as on their derivatives after protonation for use in a nanocomposite. We have to note that protonataed birnessites (monolayers birnessites) are one of the building blocks used to obtained nanocomposite supercapacitors[10-14-15]. Thus, surface reactivity investigation of protonated birnessite with different morphology and thickness are the key to rely the electrochemical performances and storage mechanisms (surface charge storage by faradaic reaction and bulk pseudocapacitive reaction redox reactions associated to faradaic mechanism and surface adsorption associated to capacitive mechanism) to the birnessite structural criteria (nature of the surface active sites (redox and/or acidbase), specific surface area, etc..).

To get deeper in the understanding of the factors that impact the capacity of the material, a multi-scale study was conducted to investigate in detail the morphology, surface reactivity, nature of active sites and identification of mechanisms involved in the storage of charges for each material. The materials will be compared characteristic by characteristic in order to understand the impact of each on the electrochemical properties. To do this, scanning electron microscopy (SEM) was used to highlight the morphology of the materials. SO_2 gas probe adsorptions were performed to probe the surface active sites of the birnessites. X-ray photoelectron spectroscopy (XPS) was used to both characterize the surface of the materials before and after adsorption and to determine and quantify the adsorption modes of SO_2 (redox-acid/base).

EXPERIMENTAL SECTION

Synthesis and bulk characterization

Synthesis method: Na-birnessite (Na-MnO_2) and K-birnessite (K-MnO_2), corresponding to manganese oxide layers with respectively sodium and potassium ions intercalated in between, are synthesized by precipitation[16]. First, 5 mmol of $MnSO_4 \cdot H_2O$ is dissolved in 15 mL of distilled water, followed by drop by drop addition of 15 mL of a strong alkaline solution (6M NaOH or KOH) under vigorous stirring. A spontaneous precipitation of a tan coloured slurry of $Mn(OH)_2$ is formed, which is then oxidized with the addition of $K_2S_2O_8$ (3.5 mmol) in order to obtain the Na-birnessite or K-birnessite. The resulting brown-black slurry is stirred for an additional 30 min, before being centrifuged and washed five times with distilled water. The brownish/black solid corresponding to Na-birnessite (or K-birnessite) is then dried at 70°C for 24h under air.

HT-MnO_2 was obtained by thermal decomposition of $KMnO_4$. 3 g of the reactant were placed in an alumina crucible and heated in a furnace under air at 800°C for 5h [17,18]. Then, the recovered powder was centrifuged 3 times in distilled water to eliminate the soluble by-products and was dried at 50°C for 24h.

The protonation step consists in a topotactic ion-exchange reaction, during which the MnO_2 slabs are preserved and the alkaline ions replaced by protons. To do so, the polycrystalline powder is suspended and stirred in HCl aqueous solution (0.1 M) for 4 days, before being recovered by centrifugation and washed with distilled water. Finally, the dark brown solid is then dried at 50°C in air for one day. The phases obtained after protonation of Na-MnO_2, K-MnO_2 and HT-MnO_2 are named H_{Na}-MnO_2, H_K-MnO_2 and H_{HT}-MnO_2 respectively.

X-ray diffraction: The X-ray powder diffraction patterns are recorded with a Philips Panalytical X'Pert Pro diffractometer using Cu-Kα radiation ($\lambda K_{\alpha 2}$= 1.540 Å, $\lambda K_{\alpha}1$= 1.544 Å). The powder diffraction patterns are recorded in the 10°−80° (2θ) angular range, with a 0.0167° (2θ) step size and a 2.022° (2θ) active width in the detector (200 s per step) for 2 hours.

ICP: Alkaline (Na and K) and Mn elements are quantified in the birnessites materials with a Varian 720ES ICP-OES spectrometer. The samples (25 mg of powder) are first dissolved into HCl, the solutions being heated in 5 mL of HCl until full dissolution of powder. Then solutions with a concentration of target element between 1 and 200 mg/L are prepared and introduced in a nebulization chamber along with an argon flow to create an aerosol. To ensure accuracy of our results, five measurements are performed for each sample.

CHNS: A Thermo Flash EA 111E Series apparatus is used to determine the carbon, hydrogen, nitrogen and sulfur elemental composition. Exactly 1.5 mg of powder is placed in the tin foil. Two measurements are performed for each sample.

Iodometric titration: The mean oxidation state of Mn is determined by using iodometric titration. We first dissolve around 30 mg of powder in a solution composed of 5 mL distilled water, 10 mL of KI solution at 10 g/L and 5 mL HCl solution at 12M (37%). Then the solution is heated to ensure the total dissolution of powder (yellowish color). Just after this step, the solution is titrated by sodium thiosulfate solution to obtain Veq, which represented the volume of added sodium thiosulfate when the yellow solution turns to transparent. The principle of iodometric titration is explained in ref [19].

BET: The analyses are performed on ASAP2010 (Micromeritics Corp., Norcross, GA, USA). The specific surfaces areas of materials are conducted by N_2 adsorption at 77K. The Brunauer-Emmett-Teller (BET) model was used to calculate the specific surface S_{BET} [20].

Surface analysis

XPS: X-ray Photoelectron Spectroscopy (XPS) analysis are performed on a Thermo K-alpha spectrometer using a focused monochromatized Al Kα radiation (hν = 1486.6eV). A Cu double tape was used to fix on the sample holder the powder materials to be analyzed. In order to avoid contaminating the samples and being in contact with the air after performing the SO_2 adsorption, the samples are prepared in a glove box and transferred into the glove box which is directly connected to the spectrometer (H_2O/O_2 < 5ppm) using a transfer vessel. A pass energy of 20 eV and an energy step of 0.1 eV are used to record the core peaks. The analysis depth is about 5 nm and the analysis area is of 200 x 400 μm^2. A neutralizer gun is used to minimize the surface charging and therefore charge compensation. XPS spectra processing and quantification are obtained using CASA XPS software with Shirley-type background subtraction. Scofield's relative sensitivity factors are used for the quantification of the surface composition [21].

SEM: Scanning electron microscopy (SEM) For Scanning electron microscopy (SEM) an Auger JEOL JAMP 9500F spectrometer was used. To analyze the surface and the core of the bare material, samples are cut with a JEOL IB-09010CP cross polisher under a controlled atmosphere of N_2. The cross polisher is located in a glove box where the atmosphere is also controlled. For realised the cross section, the sample powders are mixed with a silver conducting epoxy resin to ensure a low charge effect during acquisition and then deposited on a silicon wafer at about 250 µm thickness. The wafer and the powder-epoxy mixture are then cut with Argon plasma of 6 kV and 150 µA at 1.10^{-4} Pa during 4 hours. The cutting depth of the sample is about 150 µm. The cross-sectioned samples are then transferred from the glove box to the Auger spectrometer for analysis using a transfer vessel.

The SEM images highlight the bulk morphology of birnessite materials. The SEM is carried out under Ultra High Vacuum conditions (< 2 x 10^{-7}Pa) and an acceleration voltage of 20 keV and a current beam of 4 nA has been used. The SEM images are performed at 30° tilt to prevent charging effect.

Gas probe adsorption

The SO_2 adsorption is carried out with a Micromeritics Autochem 2920 Analyzer. The adsorptions of SO_2 gas probes are performed following four steps: the first step consists in cleaning the reactor from potentially adsorbed species by exposing it for one hour to a Helium flow at a temperature of 500°C. Then, the sample powders are introduced into the reactor (m_{powder} = 0.050 g). The second step consists in heating the device following a temperature ramp up to 80°C in order to keep the presence of water molecules between the nanosheets, still under Helium flow. During the third step, the sample is exposed to pulses of a He(80%)/(SO_2(5%)-He)(20%) gas mixture. The gas pulses of 0.5 cm^3 volume are sent every 40 seconds in a number of 35 to 120 pulses depending on the sample, until the amount of gas sent at the device inlet is the same at the outlet. This means that the SO_2 molecules are no more adsorbed on the sample and therefore that all its active sites have reacted. Finally, the last step consists in cooling down the device to the ambient temperature. After adsorption, the sample powders are directly transferred and stored in a glove box under controlled atmosphere until it is analysed. The adsorption of SO_2 gas probes allows to quantify and to determine the nature of the active sites on the surface, either acid-base or redox. For this, if SO_2 molecules are adsorbed on the surface as sulfite species (SO_3^{2-}), the active sites are basic and if SO_2 molecules are adsorbed as sulfate species (SO_4^{2-}), the active sites are oxidizing. The quantity of adsorbed species is determined from XPS analysis from the area ratio

between the S 2p and the Co 2p core peaks. The adsorption mode is assigned depending on the S 2p core peak binding energy. A binding energy (B.E.) of the S $2p_{3/2}$ core peak at 167.5 eV is characteristic of sulfite species and a B.E. of 169.0 eV is characteristic of sulfate species[22]. Due to the ultra-high vacuum conditions of XPS analyses, only the chemisorbed species are detected since the physisorbed species involve interactions that are too weak for these analytical conditions.

Electrochemical tests

The electrodes were made by mixing the active material, carbon black and PTFE following the weight ratio 80/15/5 into a motar. All the components were mixed until the formation of a self-supported black paste. This later was further rolled and a electrode was cut using a round cutter. The average mass loading of the electrode is 10 mg/cm². Electrochemical measurements were carried out in a solution of 0.5 M K_2SO_4 in a 3-electrodes configuration at 25°C. Ag/AgCl electrode and a platinum wire were respectively used as the reference electrode and the counter electrode.

In this manuscript, the capacitance values were calculated by EC-lab software from cyclic voltammetry by integrating the area under the CV charge or discharge curve. We also verified the capacity values with our own calculations.

The capacity using cyclic voltammetry can be obtained thanks to this formula:

$Cp = A / (2k.m.\Delta V)$ where A is the area under the curve (mA.V), k is the scan rate (mV/s), m the mass of active material (mg) and ΔV the potential windows (V).

The CV curves were plotted on Origin and the area under the curve was integrated using Origin software. The values obtained were in good agreement with those directly calculated by EcLab software, then we considered these latter capacity values.

RESULTS

Crystallographic structure

Birnessite is the common name given to the layered manganese oxide polymorph, δ-MnO_2. Its structure consists of layers made of edge-sharing MnO_6 octahedra separated by interlamellar alkaline cations (K^+, Na^+), protons and water molecules. X-ray diffraction patterns were recorded for the prepared materials in order to check the structure in comparison with data that were already published by numerous works[23, 24]. The indexation of the XRD patterns is reported in Figure 1 but the structural study of the materials, already performed by many authors, was not the purpose of this paper. The cell parameters and space group are listed in the Table 1. Na-MnO_2 and K-MnO_2 crystallize in a monoclinic cell with the C2/m space group while HT-MnO_2 crystallizes in a hexagonal cell with the P63/mmc space group. The diagram of K-MnO_2 exhibits wider and less defined diffraction peaks[10] than for the two other alkaline birnessites. This can be correlated to the fact that, for K-MnO_2, the structure is disordered and the coherent domains are significantly smaller comparing with Na-MnO_2 and HT-MnO_2, as reported in section 2.

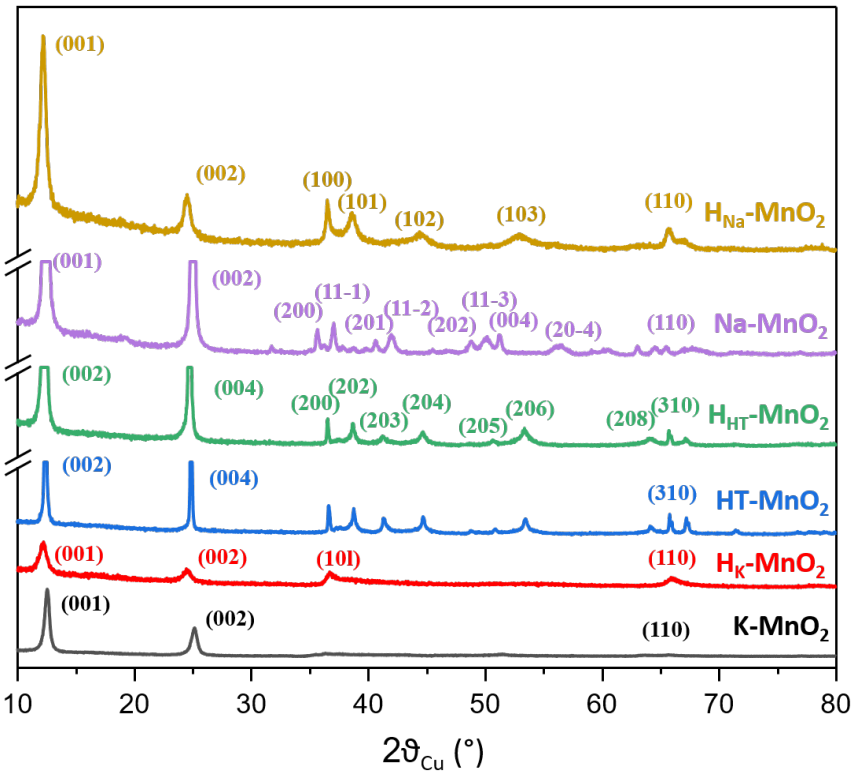

Figure 1. X-ray diffraction patterns of pristine Na-MnO_2, HT-MnO_2 and K-MnO_2, and their protonated deriving phases.

Table 1. Cell parameters of the pristine synthesized birnessites and the protonated derivatives.

	Space group	a (Å)	b (Å)	c (Å)	β (°)
K-MnO_2	C2/m	5.166(7)	2.911(6)	7.089(7)	90.8(1)
H_K-MnO_2	C2/m	2.836(3)	2.836(3)	7.32(2)	
Na-MnO_2	C2/m	5.223(6)	2.750(3)	7.286(6)	102.29(9)
H_{Na}-MnO_2	C2/m	2.839(2)	2.839(2)	7.27(1)	
HT-MnO_2	P63/mmc	2.860(4)	2.860(4)	14.24(4)	
H_{HT}-MnO_2	P63/mmc	2.837(1)	2.837(1)	14.40(8)	

As shown by the inter-reticular distance of the line at the lowest angle (001) corresponding to the interlamellar distance, the interslab distance in K-MnO_2 and HT-MnO_2, both containing intercalated K^+ ions, is slightly shorter than in Na-MnO_2. This is at first sight counter intuitive because, in size, potassium ions are much bigger than sodium ions: their ionic radius is 1.51 Å, compared to 0.99 Å for sodium[25]. However, the polarizing character, which is estimated by charge/size ratio, is higher for Na^+ than for K^+. This induces a larger hydration shell around the Na^+ cation, which conducts to an enlargement of the interslab space.

The protonation step does not affect the general shape of the X-ray diffraction patterns. We may thus suggest that the lamellar structure of the birnessite materials are maintained, while the size of coherent domains, linked to the width of the diffraction lines, is barely modified. The protons are exchanged with Na^+ and K^+ cations in the interlayers, which leads to the increase of the inter-layer distances (0.12 Å starting from Na-MnO_2 and K-MnO_2, and 0.10 Å starting from HT-MnO_2). An increase of the peak width has also to be noticed after protonation for Na-MnO_2, which suggests size decrease of the coherent domains for this material.

The accurate compositions of the birnessites series have been determined by combining ICP-OES, iodometric titrations and CHNS analyses which allow to determine respectively the cationic content (Na, K, Mn), the manganese mean oxidation state and the hydrogen content (proton + water). In the case of Na-MnO_2 and K-MnO_2 (Table 2), the results confirm that, during the protonation reaction, the Na(K)/Mn ratio drops while the H/Mn ratio increases, showing the efficient exchange of alkaline ions for protons. Moreover, the average oxidation state of manganese is increasing during protonation, from 3.53 to 3.65 in the case of Na-MnO_2 and from 3.52 to 3.63 in the case of K-MnO_2. The behaviour of the HT-MnO_2 is completely different from

the previous phases. The potassium/proton exchange is only partial, and the increase of the manganese oxidation state is not significant.

Table 2. Chemical composition and specific area of the pristine synthesized birnessites and the protonated derivatives.

Materials	Chemical composition	Specific area (m^2/g)
Na-MnO_2	$H_{0.15}^{+}Na_{0.32}^{+}(H_2O)_{0.45}Mn^{3.53+}O_2$	35
H_{Na}-MnO_2	$H_{0.34}^{+}Na_{0.01}^{+}(H_2O)_{0.39}Mn^{3.65+}O_2$	60
K-MnO_2	$H_{0.23}^{+}K_{0.25}^{+}(H_2O)_{0.34}Mn^{3.52+}O_2$	45
H_K-MnO_2	$H_{0.35}^{+}K_{0.02}^{+}(H_2O)_{0.35}Mn^{3.63+}O_2$	85
HT-MnO_2	$K_{0.30}^{+}(H_2O)_{0.32}Mn^{3.70+}O_2$	4
H_{HT}-MnO_2	$H_{0.20}^{+}K_{0.08}^{+}(H_2O)_{0.42}Mn^{3.72+}O_2$	18

Morphology

For all the studied compounds, the morphologies and the arrangement of particles within their aggregates are illustrated in Figure 2. For K-MnO_2 presented in figure 2.a, the SEM image shows a morphology that looks like folded and aggregated veils between them[10]. Due to the structure of these aggregates, the determination of the size of the veils is difficult. In order to go deeper into the morphological study of these materials, SEM images were made on samples cut with a cross-polisher. The coupling of the two methods allows having information on both the surface and the core of the materials. The cross sections image of the K-MnO_2 material (figure 2.d) shows the veils rolled up one with each other, which makes it them difficult to be distinguished. Compared to the SEM image made on an uncut sample, the cross section image still shows a relatively compact arrangement in the core of the aggregates. On the other hand, the morphology is very different for the HT-MnO_2 material (figure 2.b). The SEM image reveals a macroporous three-dimension

network. The objects are much denser and larger than in the previous material with a particle size between 1 and 15 µm. Moreover, we have also found large particles (dark grey) as reported in the SEM image on cross section (figure 2.e) of about 15 µm in diameter. The platelets are not identifiable and no porosity is observed in agreement with the BET surface (4 $\mu m^2/g$). The light grey particles correspond to the metallic epoxy used during the preparation of the sample to make the cross section. A third morphology is observed for Na-MnO_2. The corresponding SEM image (figure 2.c) shows platelets of irregular size and shape that are essentially of the order of several hundred nanometers in length[10]. The cross section image (figure 2.f) highlights the regular stacking of the MnO_2 platelets for the edges of the platelets are clearly visible.

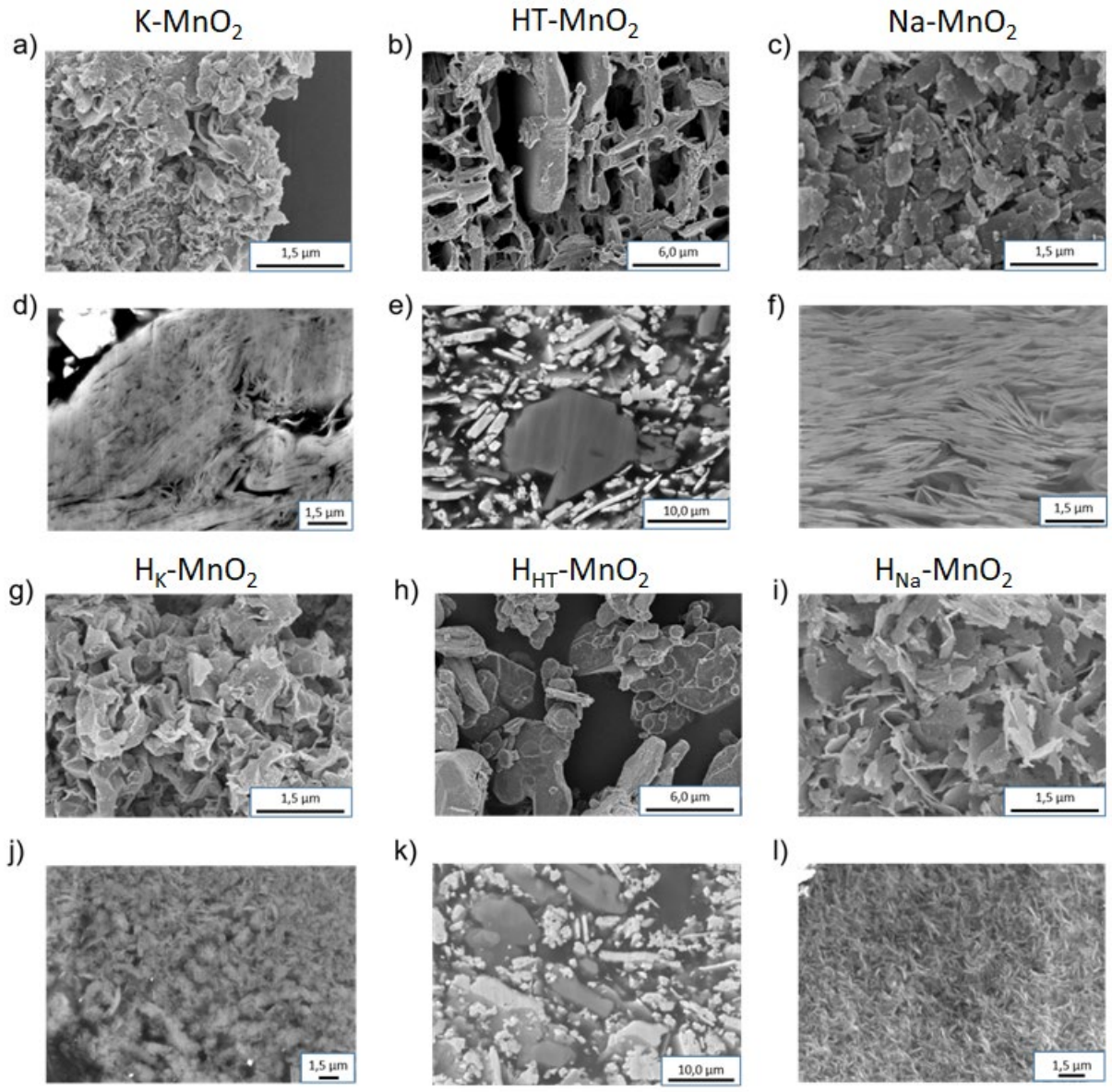

Figure 2. a), b), c) SEM images and d), e), f) cross section SEM images of K-MnO_2, HT-MnO_2 and Na-MnO_2 respectively; g), h), i) SEM images and j),k),l) cross section SEM images of the H_K-MnO_2, H_{HT}-MnO_2 and H_{Na}-MnO_2 protonated phases respectively.

After protonation, the impact on the morphology of the materials depends of the composition. In the case of H_K-MnO_2, the veil-like morphology of the material is maintained but the particles seem eroded (figure 2.g). The cross section image (figure 2.j) brings out the aggregation of the veils to form small clusters of several tens of micrometers after the protonation. For H_{HT}-MnO_2,

the structure is completely modified. The initial three-dimensional network has been broken. Thus, the particles are now disconnected from each other (figure 2.h). However, we can observed on the cross section image (figure 2.k) that the size of the primary particles are preserved.

In contrast, no major modification is observed for H_{Na}-MnO_2, except the erosion of the edges of the platelets particles (figure 2.i) such as for the H_K-MnO_2 veils. The erosion comes from the dissolution of the edges by the acidic medium during protonation. From the cross section images (Figure 2.l), we can easily observed that the particles become randomly oriented after protonation and appear more porous.

To resume, the protonation step has an impact on the initial morphology of the materials. For H_K-MnO_2 and H_{Na}-MnO_2, the protonation erodes the edge of the veils/platelets, due to the acidic environment in which the protonation is performed, and turns the arrangement of the veils/platelets from stacked particles along the same direction toward randomly orientated within aggregates. Dealing with large particles as for H_{HT}-MnO_2, the protonation breaks the 3D network formed by the particles without affecting the morphology of the primary particles.

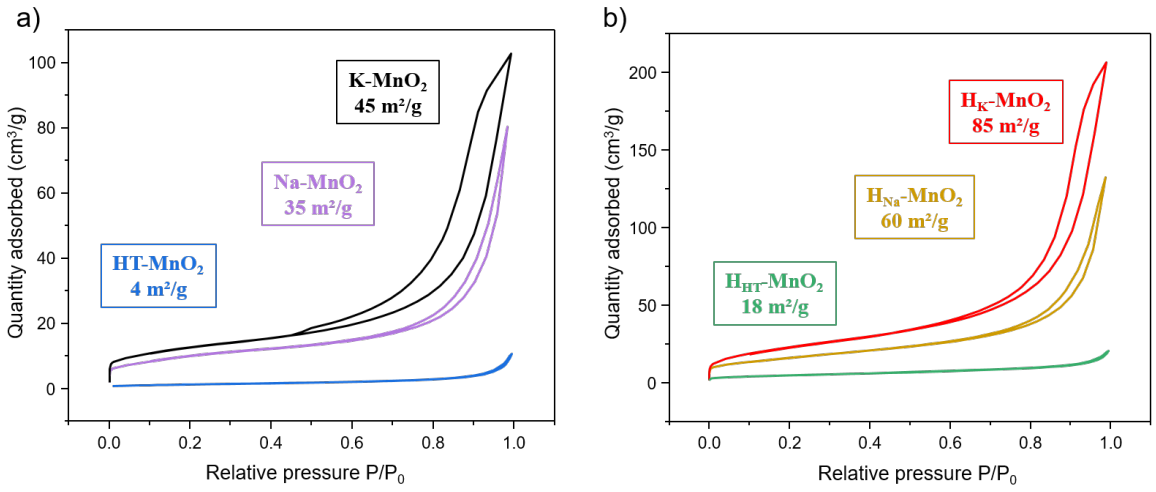

Figure 3. N_2 adsorption/desorption isotherms at 77K for bare birnessites (a): Na-MnO_2, HT-MnO_2 and K-MnO_2 and protonated derivatives (b).

Figure 3 presents the N_2 adsorption/desorption isotherms obtained for non-protonated and protonated manganese oxides. According to the classification established by Sing et al. [26], the isotherm curves of non-protonated and protonated Na-MnO_2 and K-MnO_2 can be classified in type IV category. Thus, it would correspond to mesoporous materials (pore size from 2 to 50 nm). On the other hand, HT-MnO_2 and H_{HT}-MnO_2 are identified as non-porous materials, which might be a factor explaining the difficulty to protonate HT-MnO_2. From these curves, the specific surface of each material can be determined with the BET method (Table 2).

Among the three alkaline birnessites, K-MnO_2 (45 m^2/g) exhibits the higher specific surface. Specific area of 35 m^2/g is obtained for Na-MnO_2. As it could be expected from the high temperature synthesis conditions, HT-MnO_2 presents a specific surface area almost 10 times smaller (4 m^2/g) than the two other birnessites, in accordance with its very different morphology. After protonation, the specific surfaces areas are strongly increased for all birnessites, almost twice. Tang et al.[10] have explained those results based on the partial delamination of the particles during the protonation process. Moreover, the effect of an acidic medium, which tends to "nibble" the surface of the particles, has also to be taken into account. From our SEM investigation, the increase of BET surface area is correlated with the break of 3D network for the HT-MnO_2, the erosion and the disordered stacking of the veils and platelets particles, i.e. H_K-MnO_2 and H_{Na}-MnO_2. Finally, it is observed that the protonation does not really impact the porosity of platelet birnessites (Na-MnO_2 and HT-MnO_2) but slightly increases the mesoporosity of veil birnessite by creating a population of small mesopore (Figure S1).

Electrochemical performance

Figure 4 presents the cyclic voltammetry curves for the δ-MnO_2 (a), c) and e)) series and the corresponding protonated phases (b), d) and f)) measured in 0.5M K_2SO_4 aqueous solution at

various sweep rates. Figure 5 summarizes the evolution of the specific capacity for all the electrode materials depending on the applied sweep rate.

At 0.5 mV/s, the three alkaline birnessite electrode materials exhibit a pseudo rectangular profile typical of pseudocapacitive materials in which reversible redox peaks can be distinguished (Figure 4a). These peaks are currently assigned to intercalation/deintercalation of alkaline ions into/from the interslab space through a faradaic process. These peaks are sharper and more intense for HT-MnO_2, suggesting a more important "bulk" redox contribution than for the K-MnO_2 and Na-MnO_2, which leads to a slightly higher capacity for the manganese oxide obtained at high temperature (143.4 F/g for HT-MnO_2 versus 131.6 F/g and 125.7 F/g for K-MnO_2 and Na-MnO_2 respectively (Figure 5). Although the redox peaks become broader at 5 mV/s (Figure 4 c)), the same trend is observed within the series. At higher rate (Figure 4 e)), the rectangular shape turns to an ellipse for all alkaline birnessites and the redox peaks could not be distinguished anymore due to the resistance becoming more dominant in the electrochemical response. Moreover, the poor conductivity of the birnessites prevent fast intercalation and thus, bulk redox reactions. At 100 mV/s, Na-MnO_2 exhibits the best capacity (36.6 F/g), above HT-MnO_2 (26.3 F/g) and K-MnO_2 (23.1 F/g) (Figure 5). These results clearly show that although surface reactions (redox and adsorption mechanisms) are preponderant in the charge storage, the electrochemical performances are not directly proportional to the specific surface area measured previously. Indeed, HT-MnO_2 possesses more than 10 times lower BET surface area than K-MnO_2 whereas it delivers higher specific capacity in similar experimental conditions, including at high sweep rate.

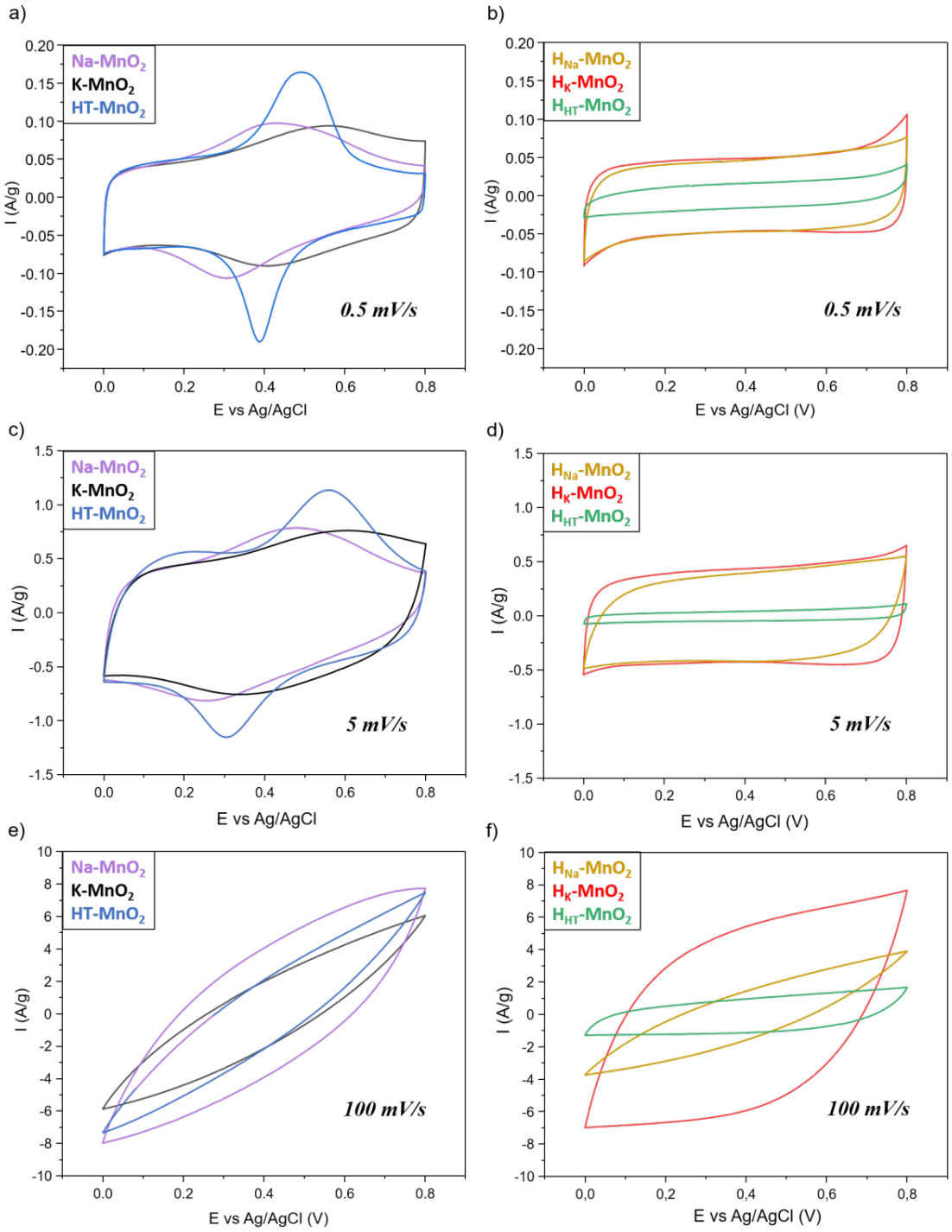

Figure **4.** Cyclic voltammograms of non-protonated and protonated birnessites obtained at 0.5 mV/s (a) and (b), 5 mV/s (c) and (d) and 100 mV/s (e) et (f) in 0.5M K_2SO_4.

After protonation, all electrode materials exhibit a well-defined rectangular shape without any redox peak, at low and moderate sweep rates (figures 4b) and 4d)). Besides the change of CV curve profile, the capacity of the protonated H_K-MnO_2 and H_{Na}-MnO_2 dropped by 20-30 % compared to their alkaline counterparts. More surprisingly, the specific capacity of HT-MnO_2 is divided, after protonation, by more than a factor 4 (e.g 143.4 F/g vs 28.5 F/g and 125.9 F/g vs 20.7 F/g at 0.5 mV/s and 5 mV/s, respectively). This huge capacity drop is completely relied with the important structural/morphological changes reported in the previous part. Finally, H_K-MnO_2 and H_{Na}-MnO_2 deliver comparable capacities, much higher than that measured for H_{HT}-MnO_2. At 100 mV/s, H_K-MnO_2 shows the best performance, and even better than for the corresponding non-protonated material. Its cyclic voltammetry profile remains rather rectangular whereas that of H_{Na}-MnO_2 becomes an ellipse. Concerning H_{HT}-MnO_2, its profile remains unchanged.

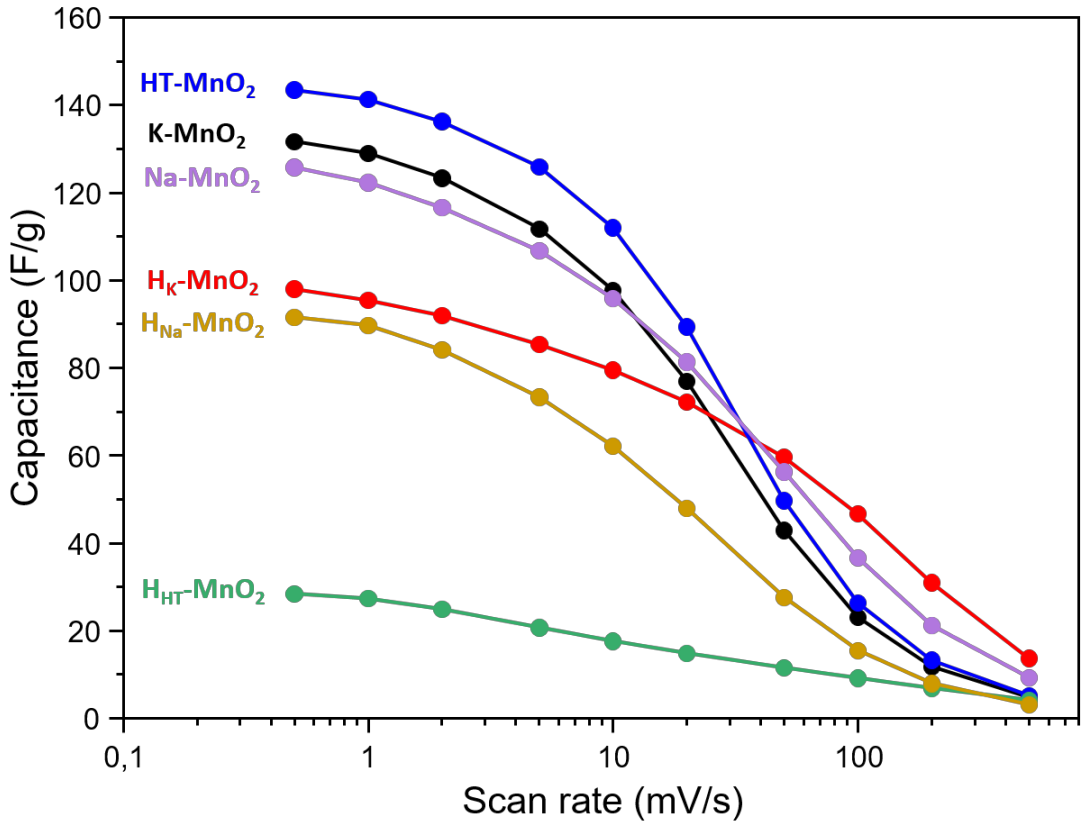

Figure 5. Variation of capacitance vs scan rate obtained for non-protonated and protonated birnessite materials.

The results presented in Figure 5 confirm that protonation globally leads to decrease the performance at low and moderate rates, even if it increases the interlayered spacing, promoting thus a possible cationic intercalation, and increases the specific surface area. On the other hand, at sweep rates higher than 50 mV/s, H_K-MnO_2 exhibits the best capacities most probably thanks to its high specific surface area. The galvanostatic charge and discharge tests are presented Figure S2 and lead to the same conclusions. The alkaline birnessite deliver higher specific capacity at low current density whereas from 5 A/g, H_K-MnO_2 exhibits a much higher specific capacity than all the other birnessites.

In conclusion, the electrochemical study shows that, at high scan rate, the material that presents the best electrochemical performances after protonation is H_K-MnO_2 with a capacitance of 40 F/g as a reason of its highest specific surface.

The next part of the study aims at determining the active sites engaged in the storage mechanism through the coupling between gaseous probe adsorption and XPS experiments. A correlation between the surface reactivity of the samples, the specific surfaces and the electrochemical properties will then be attempted.

Surface characterization

In this part, we will present the surface characterization of materials before and after protonation.

Before protonation

Before studying the surface reactivity of the different materials, they were first characterized using the XPS technique, before and after protonation. The XPS spectra obtained for the materials before protonation are presented in figure 6 and the spectra of the materials after protonation in

figure S3. All spectra in this study were calibrated from the contamination carbon at 285.0 eV present in the C 1s spectra (not shown here). For each sample, the XPS spectra of Mn 2p, O 1s and Na 1s or K 2p are presented.

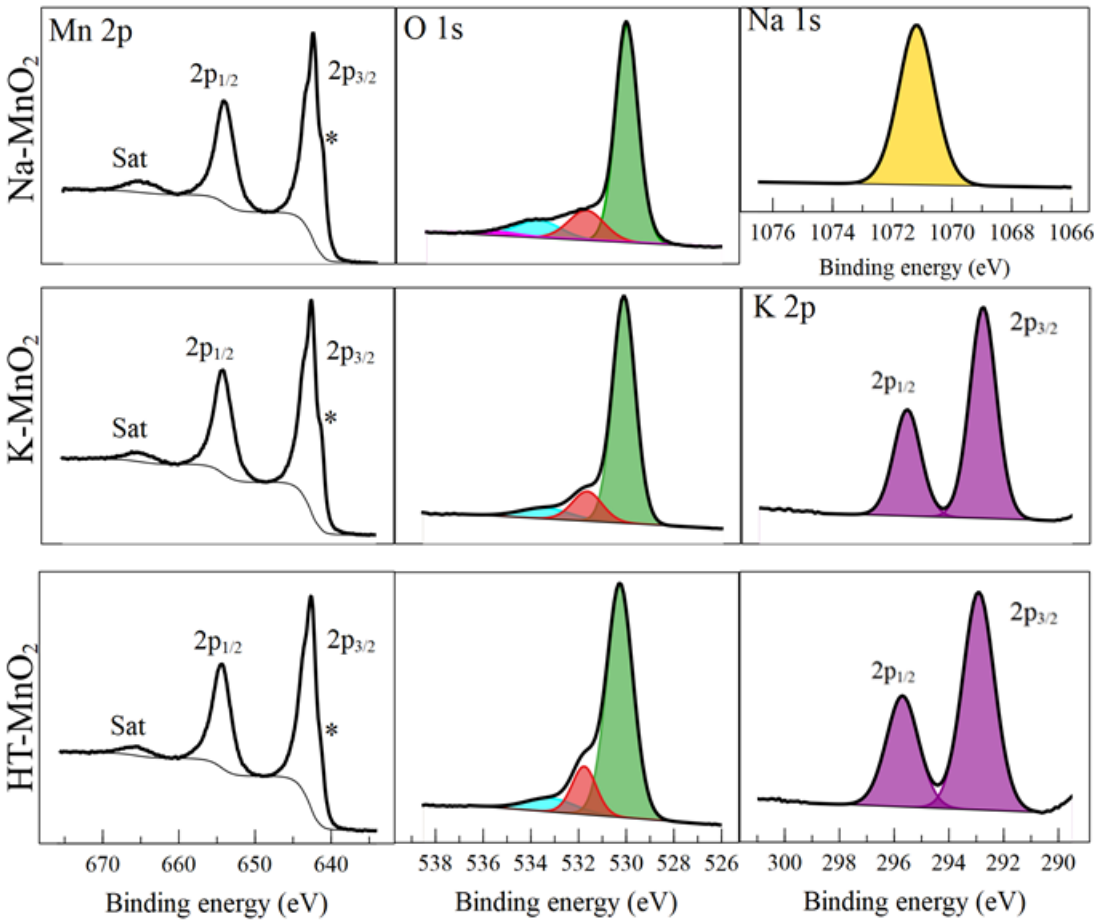

Figure 6. Mn 2p, O 1s (green: oxide anion, red: adsorbed hydroxide and under coordinated oxide, blue: water and adsorbed species and pink: Na 1s Auger) and alkaline core peaks (Na 1s or K 2p) of the Na-MnO_2, K-MnO_2 and HT-MnO_2 materials.

For the Mn 2p spectra of the materials before protonation (figure 6), three peaks are observed, two resulting from spin-orbit coupling at 642.5 eV for Mn $2p_{3/2}$ and 654.2 eV for Mn $2p_{1/2}$. The third peak at 665.0 eV corresponds to the "shake-up" satellite peak associated with Mn $2p_{1/2}$ while that of Mn $2p_{3/2}$ is merged with the Mn $2p_{1/2}$ peak. A shoulder is visible on the Mn $2p_{3/2}$ at 641.5

eV (*) which suggests the presence of a mixed valence $Mn^{4+/3+}$. It is possible to determine the oxidation state by using known references for manganese in a octahedral environment with an oxidation state of +IV, +III or +II [27,28]. The decomposition of the Mn 2p spectrum with these references allows to confirm the mixed valence Mn^{3+} and Mn^{4+} [29](see figure S4). The Mn^{3+}/Mn^{4+} ratios determined for all samples are given in Table 3. The Mn mixed valence can also been confirmed by the B.E. splitting value of the Mn 3s core peak. It is known that the $\Delta B.E._{Mn3s}$ value of the multiplet splitting is directly related to the oxidation state, i.e., the $\Delta B.E._{Mn3s}$ value for Mn^{4+}, Mn^{3+} and Mn^{2+} are 4.5 eV, 5.5 eV and 6.5 eV, respectively. In our birnessite materials, the splitting value in the Mn 3s spectra (see figure S5) are: $\Delta B.E._{Mn3s}$ = 4.8 eV for Na-MnO_2, $\Delta B.E._{Mn3s}$ = 4.7 eV for K-MnO_2 and $\Delta B.E._{Mn3s}$ = 4.6 eV for HT-MnO_2. As a result, the mixed Mn^{4+}/Mn^{3+} valence is confirmed, with a larger contribution of the Mn^{4+} in the HT-MnO_2 material. The manganese oxidation states of the materials before protonation could also be determined by XPS with the Mn 2p spectra and are as follows: Na-$Mn^{+3.56}O_2$, K-$Mn^{+3.58}O_2$, HT-$Mn^{+3.66}O_2$. These results are in agreement with the tendencies obtained with the Mn 3s spectra. Moreover, these results extracted from exploitation of Mn 2p spectra corroborate the oxidation states values from ICP measurements for which we obtained the following values: Na-$Mn^{+3.53}O_2$, K-$Mn^{+3.52}O_2$, HT-$Mn^{+3.70}O_2$.

For the O 1s spectra, for all materials, three components are observed at 530.0 eV, 531.6 eV and 533.4 eV. The component at 530.0 eV is attributed to the bulk O^{2-} oxygens, the one at 531.6 eV to the adsorbed -OH species as well as to the under-coordinated surface oxygens and finally the component at 533.5 eV is assigned to the adsorbed species and to water molecules that are trapped between the nanosheets of the materials. For Na-MnO_2, the presence of sodium ion is detected as expected. The Auger peak of Na 1s is present at 536.0 eV on the O 1s spectrum (pink component).

<u>After protonation</u>

The Mn 2p, O 1s and Na 1s or K 2p XPS spectra of the materials after protonation are shown in figure S1. The same accuracy method as mentioned just before was used to determine the manganese oxidation state, in order to follow the protonation impact on the material and their electronic structure. The Mn^{4+}/Mn ratios are presented in table 3. The ratios (0.72 for H_K-MnO_2, 0.69 for H_{Na}-MnO_2 and 0.66 for H_{HT}-MnO_2, against 0.58 for K-MnO_2, 0.56 for Na-MnO_2 and 0.66 for HT-MnO_2) indicate that the amount of Mn^{4+} increases after protonation of K-MnO_2 and Na-MnO_2, while it is maintained for HT-MnO_2. The tendency toward an increase of the oxidation state after protonation is confirmed by the evolution of the $\Delta B.E._{Mn3s}$ splitting values, from 4.8 eV and 4.7 eV for Na-MnO_2 and K-MnO_2 respectively toward 4.5 eV for H_{Na}-MnO_2 and H_K-MnO_2. This means, according to the references, that the protonation induces an increase of the Mn^{4+}/Mn^{3+} ratios, as it was deduced by iodometric titration. One of the hypotheses to explain this slight oxidation takes place in the dissolution of the edges of the sheets of these two materials when there are placed in the acidic environment of the protonation step. On the other hand, for H_{HT}-MnO_2 the large size of platelets inhibits the dissolution process and therefore the oxidation.

The success of the protonation step is confirmed by the decrease of the Na/Mn and K/Mn ratio values after protonation (almost divided by 10 (table S1)). We can notice also that protonation increases the contribution of the components associated to the under-coordinated oxygens and the adsorbed hydroxide to the whole O 1s signal. In fact, an increase of the –OH groups is expected after protonation. Especially, the atomic percentages of $O_{531.7}$ component give an increase of 100% for H_{Na}-MnO_2 and H_K-MnO_2 but only 30% for H_{HT}-MnO_2. In that case, the protonation does not impact in a same manner the three birnessites. In particularly, the H_{HT}-MnO_2 particles are not eroded after protonation.

To sum up, the protonation method is more effective for H_K-MnO_2 and H_{Na}-MnO_2 than for H_{HT}-MnO_2, which leads to a stronger impact in terms of oxidation of the surface manganese ions and of increase of surface hydroxyl groups amount.

Investigation of surface reactivity

To study the surface reactivity, gas probe adsorptions of SO_2 were performed. The objective of this reactivity study is to investigate 1) the correlation between the adsorption capacity to the birnessite morphology and the impact of the protonation on it and 2) the adsorption mechanism and the active site concentration in chemisorption conditions.

Before protonation

First, adsorption of SO_2 molecules with a number of pulses until saturation of the actives sites has been performed on the pristine birnessites. In that case, the number of pulses depends on the whole active sites available at the surface engaged in both physisorption or chemisorption mechanism. We obtain that the number of pulses required to saturate the sample surface differs from one material to another, these results are presented in table 3. For the materials before protonation, 14 pulses of gas probe were required to reach the surface saturation for HT-MnO_2 samples, 20 pulses for Na-MnO_2 and 36 pulses for K-MnO_2. As expected, the larger the BET value, the higher the required number of pulses.

After adsorption of the gas probes, the samples were analyzed by XPS to quantify the active sites and determine the adsorption mechanism directly linked to the nature of the active sites. In this part, only the chemisorption process will be taken into account as the analysis chamber is under ultra-vacuum. As the adsorption does not impact the Mn 2p spectra, only the O 1s and S 2p spectra will be presented, in Figure 7 for the materials before protonation and in figure 8 after

protonation. For all materials after adsorption, well defined S 2p core peaks can be detected, confirming the SO_2 adsorption as chemisorbed species.

First of all, for the Na-MnO_2 and K-MnO_2 materials, 95% of the adsorbed species are sulphates (B.E. S2$p_{3/2}$ = 168.7 eV in figure 7) and 5% are sulfites (B.E. S 2$p_{3/2}$ = 167.0 eV), while 100% sulphate species are observed for HT-MnO_2.

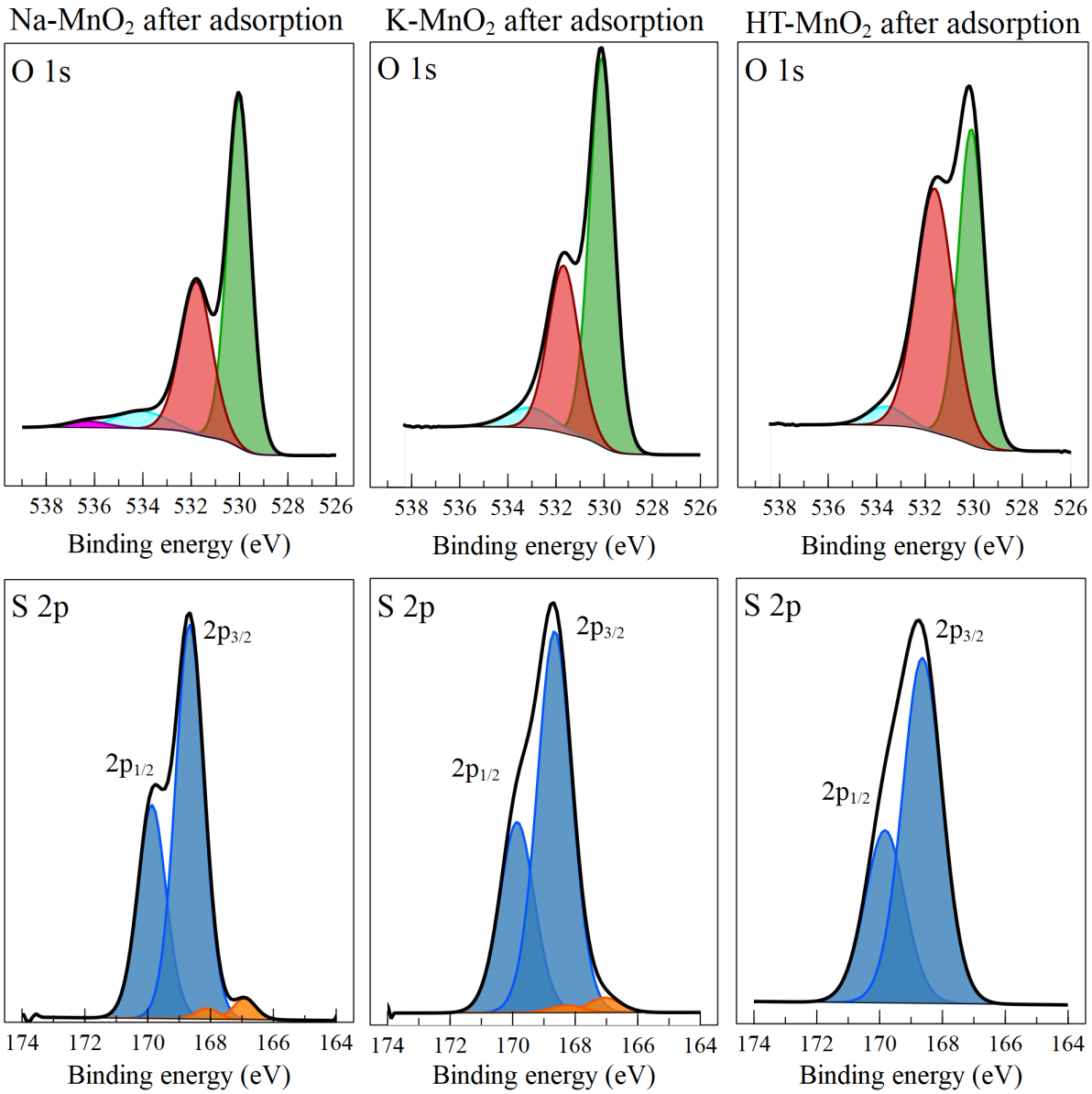

Figure 7. O 1s (green: oxide anion, red: adsorbed hydroxide, oxygen from SO_2 adsorbed and under coordinated oxide, blue: water and adsorbed species and pink: Na 1s Auger) and S 2p (blue: sulfate, orange: sulfite) core peaks of Na-MnO_2, K-MnO_2 and HT-MnO_2 materials after SO_2 adsorption.

Moreover, an increase of the $O1s_{531.7}$ component is observed according to the surface oxygen engaged in a strong bond with sulphur issued from SO_2 molecules. We found that the atomic percentage of the component located at 531.7 eV after adsorption corresponds roughly to twice the detected atomic percentage of sulphur. Indeed, for sulfate species (major contribution in our case), one sulphur is surrounded by three and four oxygens, located at 531.7 eV, including two oxygens coming from the SO_2 molecules

In terms of quantity of active sites, the S/Mn ratios are 0.31, 0.24, 0.49 for Na-MnO_2, K-MnO_2 and HT-MnO_2 respectively. As a result, before protonation, the HT-MnO_2 material, though exhibiting the smallest BET surface (5 m^2/g), has the largest surface redox sites concentration while the most divided material, i.e. K-MnO_2, exhibits the smallest redox response. This behaviour, quite counterintuitive at first sight, shows that there is no direct relation between the BET surface value and the surface reactivity of the material.

After protonation

As already observed, the number of pulses required to saturate the surface increases with the BET surface, i.e. 23 pulses for H_{HT}-MnO_2 with a BET surface of 18 m^2/g, 58 pulses for H_{Na}-MnO_2 and a BET surface of 60 m^2/g and finally 96 pulses for H_K-MnO_2 with 85 m^2/g.

Performing adsorption of SO_2 gas probes coupled with XPS on H_{Na}-MnO_2, H_K-MnO_2, and H_{HT}-MnO_2 materials allows following the impact of the protonation on the surface reactivity and especially the nature and concentration of active sites. The XPS spectra of O 1s and S 2p after adsorption are shown in figure 8. The active sites concentration that relies on the S/Mn ratio is

reported in table 3 for all birnessites. We note a slight change in terms of adsorption mechanism after protonation since the acid-base adsorption mechanism associated to formation of sulphite species is not detected, only sulfate species are indeed identified. The S/Mn ratios are evaluated as 0.21 for H_{Na}-MnO_2, 0.20 for H_K-MnO_2 and 0.46 for H_{HT}-MnO_2, respectively, against 0.31, 0.24 and 0.49 for the phases before protonation. The amounts of active sites are therefore lowered after protonation.

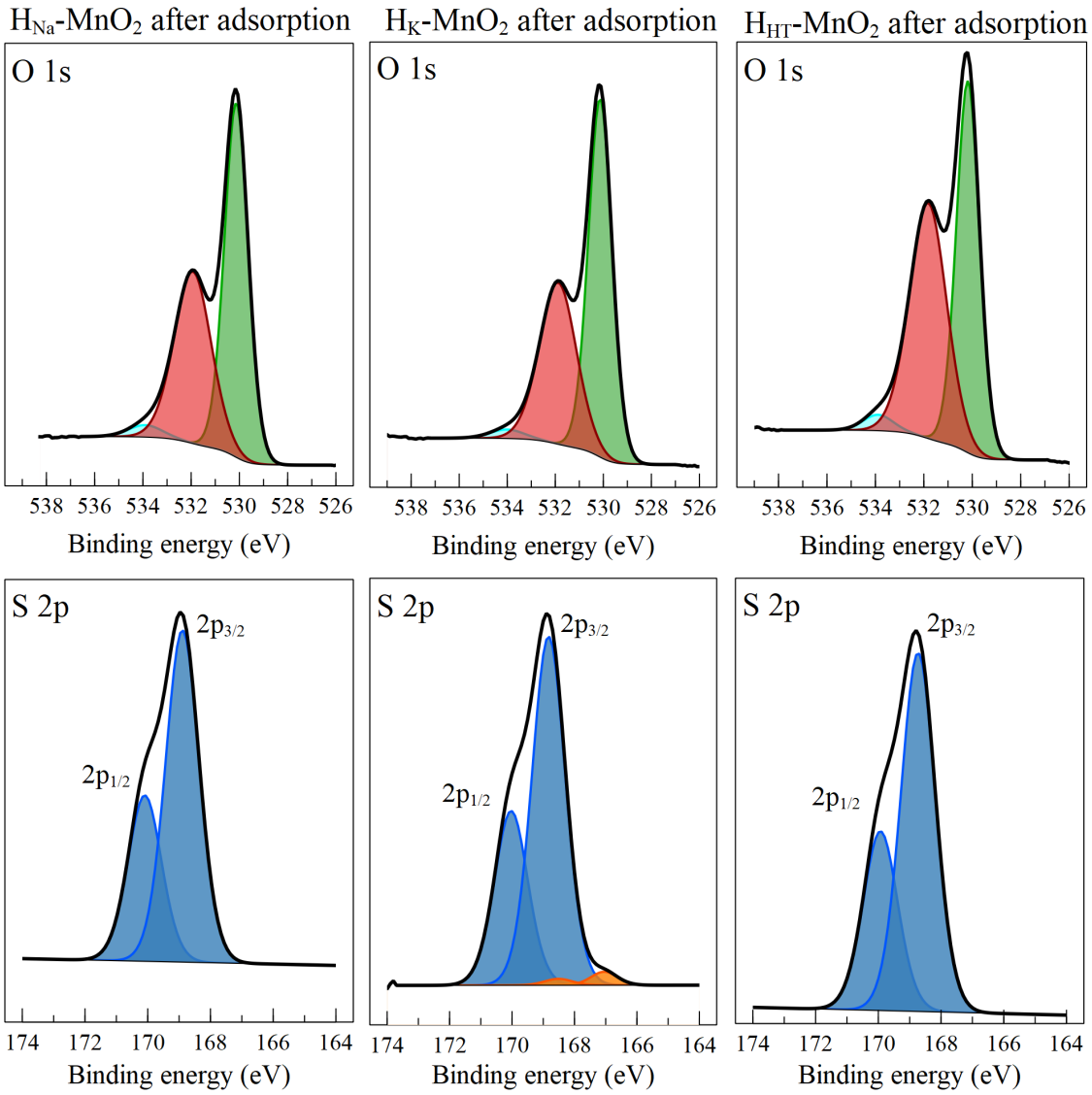

Figure 8. O 1s (green: oxide anion, red: adsorbed hydroxide, oxygen from SO_2 adsorbed and under coordinated oxide, blue: water and adsorbed species) and S 2p (blue: sulfate, orange: sulfite) core peaks of H_{Na}-MnO_2, H_K-MnO_2 and H_{HT}-MnO_2 materials after SO_2 adsorption.

Table 3. Summary of the results

	Number of SO_2 pulses to saturate the surface	BET (m^2/g)	S(at.%)/ Mn(at.%)	Sulfate/ Mn	Sulfite/ Mn	at. % S	Mn^{4+}/Mn before adsorption	Mn^{4+}/Mn after adsorption	Redox peak at 0.5 mV/s	specific capacity at 100 mV/s (F/g)
Na-MnO_2	20	35	0.31	0.3	0.01	4.9	0.56	0.36	yes	42.7
H_{Na}-MnO_2	58	60	0.21	0.21	0	4.3	0.69	0.57	no	42.7
K- MnO_2	36	45	0.24	0.23	0.01	4.5	0.58	0.56	yes	23.1
H_K- MnO_2	96	85	0.20	0.19	0.01	4	0.72	0.59	no	46.6
HT- MnO_2	14	5	0.49	0.49	0	6.3	0.66	0.59	yes	26.3
H_{HT}- MnO_2	23	18	0.46	0.46	0	6.6	0.66	0.69	no	9.2

As compared with the other two materials, in relative value, the decrease of sites concentration (S/Mn) for the HT-MnO_2 ceramic birnessite appears lower, suggesting a minor change in the surface properties for this material after protonation. We can argue that, for this material, which exhibits a weak specific surface, the exchange of protons for interlamellar K^+ cations is only partial, as revealed by the variation of K/Mn ratio before and after protonation. This behaviour can be related to the morphology, constituted of wide micrometric platelets, which develop basal surface (00l) higher than the surface corresponding to the slab edges. Because the exchange of the potassium ions by protons is more favoured on the edges of the slabs and therefore of the platelets than on the basal surface, it cannot be completed within the bulk and the platelet basal surface is not really modified, leading to a minor change in the total redox surface reactivity of the material.

From a general point of view, the tendency is that, after protonation, the number of pulses needed to saturate the surface is increasing while the amount of redox active sites (S/Mn ratio) is decreasing. We can thus conclude that the protonation i) increases the number of sites for physisorption and therefore the porosity according to the volume of the gaseous probe but ii) affects the redox adsorption mode.

DISCUSSION

It is commonly accepted that charge storage mechanisms can be divided into 3 different types: i) faradaic storage due to redox reactions linked to intercalation/deintercalation processes within the bulk of the materials, ii) pseudocapacitive storage due to redox reactions coupled to ionic adsorption on multiple sites at the surface / near surface of the materials, iii) capacitive storage corresponding to the exchange of electrostatic charges following the electrochemical double layer model[11]. The faradaic storage is not influenced by the specific surface, while the pseudocapacitive and capacitive storages are expected to be strongly dependent on it. Moreover, pseudocapacitive mechanims depends to the nature of surface active sites, especially redox sites. The present work aims at investigating the potentialities of surface reactivity measurements (by adsorption of gaseous probes coupled to XPS studies) as a key tool to predict or understand the charge storage mechanism of powdered materials.

For that purpose, six birnessite type phases with various morphologies and slightly different compositions[15] were studied in the present work: 3 pristine birnessites Na-MnO_2 (nanoplatelets), K-MnO_2 (veils) and HT-MnO_2 (large platelets of some micrometers that form a 3D network), and their 3 derivatives obtained by exchange of alkaline ions for protons, namely H_{Na}-MnO_2 (eroded nanoplatelets), H_K-MnO_2 (eroded veils) and H_{HT}-MnO_2 (still large platelets, but the 3D network linking them is destroyed). In terms of porosity, Na-MnO_2 and K-MnO_2, as well as their protonated

derivatives, can be considered as mesoporous materials, while not for HT-MnO_2 and its derivative. The largest specific surface goes to H_K-MnO_2 with its eroded veils (85 m^2/g), and the smallest to HT-MnO_2 (5 m^2/g) with its interconnected large platelets.

The adsorption of SO_2 gaseous probe performed on the various materials allows to deduce surface reactivity. First, regarding the adsorption of SO_2 molecules with a pulse mode until saturation of the surface actives sites, the number of pulses depends on the whole active sites (physisorption or chemisorption mechanism) available at the surface. It should be noted that, experimentally, for the whole series of materials, the order of the number of pulses follows quite well the order of the specific surface values. Second, regarding the S/Mn ratio determined by XPS analysis of the surface after adsorption, as a reason of the ultra-vacuum experimental conditions, it corresponds to the concentration of the surface redox sites (chemisorption mechanism). The values of this ratio appear to be the largest for, in the order, HT-MnO_2 (0.49), its protonated derivative H_{HT}-MnO_2 (0.46) and Na-MnO_2 (0.31), probably because these materials are constituted of integral and smooth platelets, favouring thus the presence of (001) surfaces. As soon as the platelets are eroded by the protonation acidic medium, which is the case of H_{Na}-MnO_2, or when the platelet morphology is replaced by veils, as in the case of K-MnO_2 and H_K-MnO_2, the concentration of redox active sites decreases (S/M ratio close to 0.2).

As far as the electrochemical properties are concerned, let us try to correlate the evolution of the capacities to the properties and characteristics listed above. At low scan rate, as shown by the shape of the voltammograms in Figure 4, the charge storage process is dominated for the 3 pristine materials by a pseudocapacitive behaviour (rectangular part) and a significant faradaic one (redox peaks) due to intercalation/deintercalation of the alkaline ions[11,15]. For the protonated derivatives, the faradaic contribution disappears because the intercalated protons hinder the

intercalation/deintercalation process of the alkaline ions. That is the reason why the capacities delivered by the protonated materials are significantly lower than those of their non protonated precursors. At this low rate, the best capacity is obtained for the material HT-MnO_2, which exhibits an intense faradaic contribution (high surface of the redox peaks), and the largest concentration of redox sites (S/M = 0.49), which can reasonably be linked to the pseudocapacitive component. It should be noted that this material exhibits thus the highest capacity, in spite of its lowest specific surface (5 m^2/g). On the contrary, at high rate, as an example for 100 mV/s, the best capacity is for the H_K-MnO_2 phase (46 F/g), which exhibits the highest specific surface (85 m^2/g). This behaviour is in accordance with the fact that, at such rate, the charge storage process is dominated by a capacitive process, which is all the more promoted as the specific surface is high[10,11]. It should be noticed that the capacity of H_{HT}-MnO_2 is particularly low with regard to other materials on the whole scan rate range. This bad performance can be assigned to the fact that i) the disconnection of the large platelets is likely to limit the inter-particle ionic and electronic transfers, thus inhibiting both the pseudocapacitive behaviour, in spite of a good concentration of redox sites (S/Mn=0.46, close to the 0.49 value observed for HT-MnO_2), and the capacitive behaviour, ii) the specific surface (18 m^2/g) is quite low, which is particularly detrimental to the capacitive behaviour iii) the faradaic intercalation-deintercalation of alkaline ions between the slabs is completely prevented by the presence of protons at the edges of the interlamellar spaces.

The main mechanisms involved after protonation of the materials are then the surface redox reactions (pseudocapacitive) and electrostatic surface adsorption (capacitive). These two mechanisms could be studied in a distinct way by varying the scan rate during the cycling as seen previously. Moreover, the results of the adsorption experiments, which allowed to determine the amount of surface active sites, can be directly linked to the contribution of the pseudocapacitive

mechanism observed at low and moderate scan rates. As for the capacitive mechanism is discriminated at high scan rate, its contribution is related to the BET surface of the material as well as to the quantity of gas probe pulses sent during the adsorption experiments. The larger the BET surface area, the larger the number of pulses sent to probe the material surface. On the other hand, the contribution of the capacitive phenomenon cannot be quantified with the XPS technique because the analyses are carried out under ultra-vacuum, thus only the chemisorbed species are still present. The BET surface is an important criterion for the capacitive phenomenon but has a moderate impact on the concentration of active redox sites on the surface, it does not directly influence the pseudocapacitive phenomenon. The electrochemically active surface appears thus different from the BET surface.

CONCLUSIONS

The objective of this work is to establish a link between the morphology and the specific surface of birnessite materials Na-MnO_2, K-MnO_2 and HT-MnO_2 and after protonation with its electrochemical behaviour. Our approach was to study the surface reactivity of the materials through adsorption of SO_2 gas probes, with XPS monitoring to identify and quantify the adsorbed species present at the materials surfaces.

It was shown that the three birnessites have different morphologies, veil-like for K-MnO_2, platelet-like for Na-MnO_2 and large platelets forming a 3D network for HT-MnO_2. By performing cyclic voltammetry curves of these materials at different scan rates, it could be observed from the shape of the curves that surface redox reactions (pseudocapacitive), bulk redox reactions (faradaic) and electrostatic adsorption (capacitive) occur. After protonation of these same materials, an evolution of the morphology is observed. Indeed, for H_{Na}-MnO_2 and H_K-MnO_2, a slight erosion of

the edges of the veils and platelets occurred due to the acidic environment in which the protonation was performed. Thanks to the probes of the surface chemical reactivity before and after protonation it could be confirmed that this erosion leads to a decrease in the quantity of redox active sites. It was also possible to observe a disappearance of bulk redox reactions following this protonation. As for the H_{HT}-MnO_2 material, the protonation led to a rupture of the 3D network and consequently the capacity was strongly reduced, well below that of H_{Na}-MnO_2 and H_K-MnO_2.

Due to its veil-like morphology, the BET surface of H_K-MnO_2 is larger than those of the other materials (85 m^2/g vs 60 m^2/g for H_{Na}-MnO_2 and 18 m^2/g for H_{HT}-MnO_2). Thus, the contribution of the capacitive mechanism is the largest in the case of H_K-MnO_2 material. The surface chemical reactivity has revealed that H_K-MnO_2 and H_{Na}-MnO_2 materials exhibit an equivalent amount of surface redox active sites, the difference in electrochemical performance can be explained by the BET surface of H_K-MnO_2 which allows a larger electrostatic charge storage. This explains why after protonation the capacity of H_K-MnO_2 is the highest.

In conclusion, the most suitable material for use as an electrode material in supercapacitor storage systems is H_K-MnO_2 because of its surface chemical reactivity, BET surface area and specific capacity.

ASSOCIATED CONTENT

Supporting Information. The Supporting information contains figures, tables and description to complete and precise some points in the main manuscript. This material is available free of charge via the Internet at http://pubs.acs.org.

Pore size distribution of the six studied birnessite. Galvanostatic charge and discharge curves obtained in 0.5M K_2SO_4 at 0.5 A/g (left) and (right) specific capacity evolution for all birnessite

in function of current density. Mn 2p, O 1s, Na 1s or K 2p XPS spectra of protonated birnessites; Deconvolution of the Mn 2p spectrum of H_{Na}-MnO_2 material from Mn^{3+} and Mn^{4+} reference materials; Mn 3s core peaks of non-protonated and protonated birnessites; detailed XPS results (identifications and quantifications) before and after protonation and after an exposure to the SO_2 pulses.

AUTHOR INFORMATION

Corresponding Author

*Delphine Flahaut

delphine.flahaut@univ-pau.fr

*Liliane Guerlou-Demourgues

liliane.Guerlou-Demourgues@enscbp.fr

ACKNOWLEDGMENTS

The authors acknowledge Saft and Région Nouvelle-Aquitaine for the funding of the project.

REFERENCES

(1) González, A.; Goikolea, E.; Barrena, J. A.; Mysyk, R. Review on Supercapacitors: Technologies and Materials. *Renew. Sustain. Energy Rev.* **2016**, *58*, 1189–1206. https://doi.org/10.1016/j.rser.2015.12.249.

(2) Simon, P.; Gogotsi, Y. Materials for Electrochemical Capacitors. *Nanosci. Technol.* **2009**, *7*, 10.

(3) Choudhary, N.; Li, C.; Moore, J.; Nagaiah, N.; Zhai, L.; Jung, Y.; Thomas, J. Asymmetric Supercapacitor Electrodes and Devices. *Adv. Mater.* **2017**, *29* (21), 1605336. https://doi.org/10.1002/adma.201605336.

(4) Shao, Y.; El-Kady, M. F.; Sun, J.; Li, Y.; Zhang, Q.; Zhu, M.; Wang, H.; Dunn, B.; Kaner, R. B. Design and Mechanisms of Asymmetric Supercapacitors. *Chem. Rev.* **2018**, *118* (18), 9233–9280. https://doi.org/10.1021/acs.chemrev.8b00252.

(5) Jiang, Y.; Liu, J. Definitions of Pseudocapacitive Materials: A Brief Review. *ENERGY Environ. Mater.* **2019**, *2* (1), 30–37. https://doi.org/10.1002/eem2.12028.

(6) Nguyen, T.; Montemor, M. de F. Metal Oxide and Hydroxide–Based Aqueous Supercapacitors: From Charge Storage Mechanisms and Functional Electrode Engineering to Need-Tailored Devices. *Adv. Sci.* **2019**, *6* (9), 1801797. https://doi.org/10.1002/advs.201801797.

(7) Lin, Z.; Goikolea, E.; Balducci, A.; Naoi, K.; Taberna, P. L.; Salanne, M.; Yushin, G.; Simon, P. Materials for Supercapacitors: When Li-Ion Battery Power Is Not Enough. *Mater. Today* **2018**, *21* (4), 419–436. https://doi.org/10.1016/j.mattod.2018.01.035.

(8) Xia, H.; Shirley Meng, Y.; Yuan, G.; Cui, C.; Lu, L. A Symmetric RuO2/RuO2 Supercapacitor Operating at 1.6 V by Using a Neutral Aqueous Electrolyte. *Electrochem. Solid-State Lett.* **2012**, *15* (4), A60. https://doi.org/10.1149/2.023204esl.

(9) Brousse, T.; Toupin, M.; Dugas, R.; Athouël, L.; Crosnier, O.; Bélanger, D. Crystalline MnO[Sub 2] as Possible Alternatives to Amorphous Compounds in Electrochemical Supercapacitors. *J. Electrochem. Soc.* **2006**, *153* (12), A2171. https://doi.org/10.1149/1.2352197.

(10) Tang, C.; Giaume, D.; Weill, F.; Penin, N.; Dourges, M.-A.; Saadaoui, H.; Guerlou-Demourgues, L. Synergy of Mn and Co in Slab-Based Nanocomposites for Hybrid Supercapacitors: Impact of Restacking Process on Electrochemical Properties. *ACS Appl. Energy Mater.* **2019**, *2* (11), 7832–7842. https://doi.org/10.1021/acsaem.9b01263.

(11) Zhu, S.; Huo, W.; Liu X.; Zhang, Y. Birnessite based nanostructures for supercapacitors: challenges, strategies and prospects, *Nanoscale Adv*. **2020**, 2, 37. https://doi.org/10.1039/C9NA00547A

(12) *De, V.V.; Pomerantseva, E.A.; Kulova, T.L.; Grigorieva, A.V.; Skundin, A.M.; Goodilin, E.A.; Tretyakova, Y.D. Synthesis, chemical modification and electrochemical behaviour of layered sodium manganese dioxide, Mendeleev Commun.* ***2009****, 19, 187–189.* https://doi.org/10.1016/j.mencom.2009.07.004

(13) Toupin, M.; Brousse, T.; Bélanger, D. Charge Storage Mechanism of MnO_2 Electrode Used in Aqueous Electrochemical Capacitor. *Chem. Mater.* **2004**, *16* (16), 3184–3190. https://doi.org/10.1021/cm049649j.

(14) Madec, L. ; Tang, C. ; Ledeuil, J.-B. ; Giaume, D. ; Guerlou-Demourgues, L. Cross-Section Auger Analysis to Study the Bulk Organization/Structure of Mn-Co Nano-Composites for Hybrid Supercapacitors. *J. Electrochem. Soc.* **2021**, 168 (1), 010508-010514. https://doi.org/10.1149/1945-7111/abd606.

(15) Thèse Céline Tang Exfoliation and restacking of manganese and cobalt based lamellar oxides for supercapacitor electrodes HAL Id: tel-01696266 https://tel.archives-ouvertes.fr/tel-01696266 Submitted on 30 Jan 2018

(16) Ching, S.; Neupane, R. P.; Gray, T. P. Synthesis and Characterization of a Layered Manganese Oxide: Materials Chemistry for the Inorganic or Instrumental Methods Lab. *J. Chem. Educ.* **2006**, *83* (11), 1674. https://doi.org/10.1021/ed083p1674.

(17) Kim, S. H.; Kim, S. J.; Oh, S. M. Preparation of Layered MnO_2 via Thermal Decomposition of $KMnO_4$ and Its Electrochemical Characterizations. *Chem. Mater.* **1999**, *11* (3), 557–563. https://doi.org/10.1021/cm9801643.

(18) Gaillot, A.-C.; Flot, D.; Drits, V. A.; Manceau, A.; Burghammer, M.; Lanson, B. Structure of Synthetic K-Rich Birnessite Obtained by High-Temperature Decomposition of $KMnO_4$. I. Two-Layer Polytype from 800 °C Experiment. *Chem. Mater.* **2003**, *15* (24), 4666–4678. https://doi.org/10.1021/cm021733g.

(19) Invernizzi, R.; Guerlou-Demourgues, L.; Weill, F.; Lemoine, A.; Dourges, M.-A.; Baraille, I.; Flahaut, D.; Olchowka, J. Controlled Nanostructuration of Cobalt Oxyhydroxide Electrode Material for Hybrid Supercapacitors. *Materials* **2021**, *14* (9), 2325. https://doi.org/10.3390/ma14092325.

(20) Emmet, P.H.; Brunauer, S.; Love, K.S. The Measurement of Surface Areas of Soils and Soil Colloids by the Use of Low Temperature Van Der Waals Adsorption Isotherms, Journal of the American Chemical Society 1938, 60(2), 309-319.

(21) Foix, D.; Sathiya, M.; McCalla, E.; Tarascon, J.-M.; Gonbeau, D. X-Ray Photoemission Spectroscopy Study of Cationic and Anionic Redox Processes in High-Capacity Li-Ion Battery Layered-Oxide Electrodes. *J. Phys. Chem. C* **2016**, *120* (2), 862–874. https://doi.org/10.1021/acs.jpcc.5b10475.

(22) Andreu, N.; Flahaut, D.; Dedryvère, R.; Minvielle, M.; Martinez, H.; Gonbeau, D. XPS Investigation of Surface Reactivity of Electrode Materials: Effect of the Transition Metal. *ACS Appl. Mater. Interfaces* **2015**, *7* (12), 6629–6636. https://doi.org/10.1021/am5089764.

(23) Drits, V. A.; Silvester, E.; Gorshkov, A. I.; Manceau, A. Structure of Synthetic Monoclinic Na-Rich Birnessite and Hexagonal Birnessite: I. Results from X-Ray Diffraction and Selected-Area Electron Diffraction. American Mineralogist 1997, 82 (9–10), 946–961.

(24) Gaillot, A.-C. Caractérisation Structurale de La Birnessite: Influence Du Protocole de Synthese, Université Joseph-Fourier-Grenoble I, 2002.

(25) R.D. Shannon. Revised Effective Ionic Radii and Systematic Studies of Interatomic Distances in Halides and Chalcogenides, Acta Crystallographica 1976, 32(5), 751-767.

(26) Lykiema, J.; Sing, K. S. W.; Haber, J.; Kerker, M.; Wolfram, E.; Block, J. H.; Churaev, N. V.; Everett, D. H.; Hansen, R. S.; Haul, R. A. W.; Hightower, J. W.; Hunter, R. J. Prepared for Publication by the Subcommittee on Reporting Gas Adsorption Data Consisting of K. S. W. SING (UK, Chairman); D. H. EVERETT (UK); R. A. W. HAUL (FRG); L. MOSCOU (Netherlands); R. A. PIEROTTI (USA); J. ROUQUEROL (France); T. SIEMIENIEWSKA (Poland). **1984**, 17.

(27) Brabers, V.A.M.; Van Setten, F.M.; Knapen, P.S.A. X-Ray Photoelectron Spectroscopy Study of the Cation Valencies in Nickel Manganite. J.Solid State Chem. 1983, 1(37), 93-98.

(28) Allen, G. C.; Harris, S. J.; Jutson, L. A study of a number of mixed transition metal oxide spinels using X-ray photoelectron spectroscopy, Appl. Surf. Sci. 1989 (37), 111-134.

(29) Quesne-Turin, A.; Flahaut, D.; Croguennec, L.; Vallverdu, G.; Allouche, J.; Charles-Blin, Y.; Chotard, J.-N.; Ménétrier, M.; Baraille, I. Surface Reactivity of Li_2MnO_3 : First-Principles

and Experimental Study. *ACS Appl. Mater. Interfaces* **2017**, *9* (50), 44222–44230. https://doi.org/10.1021/acsami.7b14826.